Diffusive and convective dissolution of carbon dioxide in a vertical cylindrical cell

Daniël P. Faasen ⬤,[*],[†] Farzan Sepahi ⬤,[*],[‡] Dominik Krug ⬤,[§] Roberto Verzicco,[‖] Pablo Peñas,
Detlef Lohse ⬤,[¶] and Devaraj van der Meer ⬤[**]

*Physics of Fluids Group, Faculty of Science and Technology, University of Twente, 7500 AE Enschede,
The Netherlands*

The dissolution and subsequent mass transfer of carbon dioxide gas into liquid barriers plays a vital role in many environmental and industrial applications. In this work, we study the downward dissolution and propagation dynamics of CO_2 into a vertical water barrier confined to a narrow vertical glass cylinder, using both experiments and direct numerical simulations. Initially, the dissolution of CO_2 results in the formation of a CO_2-rich water layer, which is denser in comparison to pure water, at the top gas-liquid interface. Continued dissolution of CO_2 into the water barrier results in the layer becoming gravitationally unstable, leading to the onset of buoyancy-driven convection and, consequently, the shedding of a buoyant plume. By adding sodium fluorescein, a pH-sensitive fluorophore, we directly visualize the dissolution and propagation of the CO_2 across the liquid barrier. Tracking the CO_2 front propagation in time results in the discovery of two distinct transport regimes, a purely diffusive regime and an enhanced diffusive regime. Using direct numerical simulations, we are able to successfully explain the propagation dynamics of these two transport regimes in this laterally strongly confined geometry, namely by disentangling the contributions of diffusion and convection to the propagation of the CO_2 front.

DOI: 10.1103/PhysRevFluids.8.093501

I. INTRODUCTION

The dissolution and subsequent mass transfer of carbon dioxide gas into liquid barriers plays a vital role in many environmental and industrial applications. In microfluidics for example, Taylor flow, a segmented flow of alternating gas and liquid plugs, is utilized in microreactor designs to increase heat and mass transfer rates, resulting in higher reactor performance [1–3]. On a larger scale, carbon capture and sequestration is often based on injecting CO_2 into deep saline aquifers, trapping the CO_2 between a layer of cap rock and a liquid reservoir, which results in the long term, stable storage of CO_2 in the aquifer [4–6].

Once the carbon dioxide starts to dissolve into the water layer, a CO_2-rich water layer forms at the interface, which is denser in comparison to pure water. While initially stable, the continued

---

[*]These authors contributed equally to this work.

[†]d.p.faasen@utwente.nl

[‡]f.sepahi@utwente.nl

[§]d.j.krug@utwente.nl

[‖]r.verzicco@utwente.nl

[¶]d.lohse@utwente.nl

[**]d.vandermeer@utwente.nl
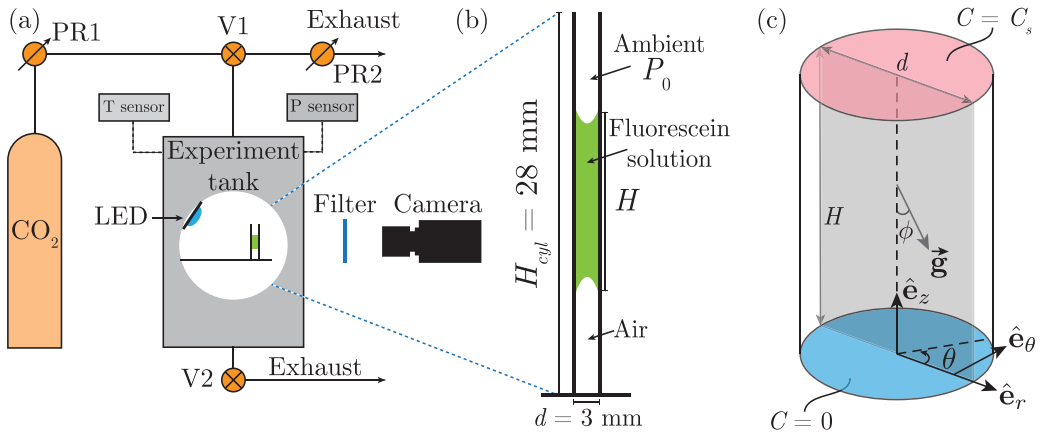
FIG. 1. (a) Schematic overview of the experimental setup. (b) Sketch of the cylinder containing the liquid-air setup. The cylinder is placed inside the experimental chamber, which is subsequently flushed with CO_2 gas. (c) Schematic overview of the numerical setup.

dissolution of CO_2 into the water layer results in the CO_2-rich fluid layer becoming gravitationally unstable, leading to the onset of buoyancy-driven convection and the formation of a buoyant plume, which greatly enhances the mass transfer of CO_2 in the water layer [7,8]. Furthermore, density-driven. convection can also occur as a result of buoyancy generating chemical reactions [9–12], droplet dissolution [13,14], and bubble growth [15,16].

In literature, studies investigating the dissolution and density-driven convection in the CO_2-water system have reported between two and four distinct transport regimes [17–19]. These regimes are vaguely defined by their assumed dominant driving mechanism and thus referred to as, for example, "purely diffusive," "early convective," or "late convective" [17]. Moreover, in the regimes where convection is contributing to the mass transport, apparent diffusive behavior is observed, albeit with a much higher effective diffusion coefficient. Depending on the experimental conditions, this effective diffusion coefficient can be several orders of magnitude bigger in comparison to the expected diffusive counterpart under similar experimental conditions [20–24]. However, little explanation has been given as to what drives the different observed regimes, the transitions between the regimes and why the system still appears to behave in a diffusive manner.

This is precisely the focus of our work. We study the dissolution and downward propagation of CO_2 into a vertical water barrier confined to a narrow cylindrical cell either above a trapped air bubble, an alkane layer or directly on top of a solid silicon plate, as shown in Fig. 1. We replace the ambient air atmosphere with a CO_2 atmosphere at the same pressure and by adding sodium fluorescein, a pH-sensitive fluorophore, to the liquid barrier, we can directly visualize the propagation of CO_2 [25–27]. We compare the experimental results to those obtained by three-dimensional (3D) direct numerical simulations in order to elucidate the relevant transport mechanisms.

In a nutshell, our aim is to investigate the mass transport mechanisms in a laterally strongly confined system after the dissolution of CO_2 into a liquid barrier. We will identify two different regimes, namely a purely diffusive regime and an enhanced diffusive regime. The direct numerical simulations allow us to disentangle the contributions of the buoyancy-driven convection and diffusion towards the front propagation velocity. We will show that the onset of convection leads to a distortion of the propagation front surface, resulting in the increase of the concentration gradients which in turn leads to enhanced diffusive fluxes. The overall behavior remains diffusive, however, although with an increased diffusion coefficient. The diffusive propagation acts to flatten the interfacial area, which over time leads to an equilibrium with the convective bulging of the front, after which the front propagates at an almost constant velocity.

This paper is organized as follows. The experimental setup and procedure are described in Sec. II. Section III presents the results of our visualization experiments. In Sec. IV the amount of CO_2 in the liquid barrier over time is investigated by first obtaining the intensity profiles from the visualization experiments and subsequently converting them to concentration profiles. In Sec. V we study the front propagation dynamics of the CO_2 layer and identify two distinct propagation regimes. In Sec. VI we provide the details on the numerical model we us to study the physics behind the front propagation dynamics and provide a comparison between the numerical model and the experiments. The paper ends with a summary of the main findings and an outlook in Sec. VII.

II. EXPERIMENTAL PROCEDURE

A schematic overview of our experimental setup is shown in Fig. 1(a). The experiments are conducted inside a sealed chamber which can be flushed with CO_2 gas. The inlet pressure is fixed to 1.0 bar using the pressure regulator PR1, whereas pressure regulator PR2 prevents overpressurization of the experimental tank. A more detailed description of the experimental chamber and pressure control system can be found elsewhere [28].

A single borosilicate glass (Duran) cylinder (28 mm in length, inner diameter $d = 3.0$ mm, outer diameter of 5.0 mm) is attached on one end to a silicon wafer plate using Loctite 4305 (Farnell), in an almost perfectly vertical manner, while the other end is left open. Before use, the cylinder is rinsed using ethanol (Boom, technical grade) followed by Milli-Q water (resistivity = 18.2 MΩ cm) and finally dried in a nitrogen stream.

We prepare the cylinder in one of three different configurations, a liquid-solid, liquid-liquid, or a liquid-air configuration, as depicted in Fig. 1(b). In all configurations, a layer of a 10^{-4} M aqueous fluoroscein solution is injected into the cylinder, at a volume of $V = 120$ μl (or $H \approx 18$ mm), which acts as the liquid barrier. This solution is freshly prepared prior to the experiments by adding sodium fluorescein salt (Fisher Scientific, general purpose grade) to Milli-Q water. Fluoroscein is a well-known fluorophore often used in biological application, with its main absorbance peak at 490 nm and main emission peak at 513 nm [25–27]. More importantly, the emission intensity of fluorescein has a (nonlinear) dependency on the pH level of the liquid, allowing us to follow the dissolution and propagation of the CO_2 in the liquid. Furthermore, the presence of the sodium fluorescein in the barrier does not affect the diffusive and convective behavior of the CO_2, as we have ~4.4 μg sodium fluorescein in the 120-μl barrier to achieve the desired concentration.

For the liquid-air configuration, the fluorescein layer is placed in the cylinder such that a bubble of arbitrary height spanning the entire width of the cylinder, is trapped underneath the liquid. The liquid barrier remains in place due to a stable balance between the surface tension of the liquid-air interface, the weight of the liquid barrier, and the differences in gas pressures. Since the surface tensions of CO_2 and air above water are almost identical, the force balance persists throughout our experiments [29]. For the liquid-solid configuration, the fluoroscein solution is injected into the cylinder such that no air is trapped between the liquid barrier and the silicon wafer plate. During this process, special attention is paid to ensure no small bubbles are entrained at the liquid-solid interface. Finally, for the liquid-liquid interface, 60 μl n-hexadecane (VWR, 99% purity) is injected first into the cylinder. On top of this liquid layer, the fluorescein solution is carefully injected, again to prevent the entrapment of bubbles. Despite the density of n-hexadecane being lower compared to the density of water, this configuration remains stable during our experiments, again due to a stable balance between the surface tensions at the interface and the weight of the top liquid column.

Inside the tank, an LED (Thorlabs, $\lambda_{\text{center}} = 470$ nm) is located to illuminate the cylinder, while the pressure and temperature sensors in the chamber record the pressure P_0 and temperature T in time, respectively (1 acquisition per second). The average temperature during our experiments is determined to be $T = 22.3 \pm 0.4$ °C. We use a Nikon D850 camera in silent interval timer shooting mode (1 fps) in combination with a Zeiss Makro Planar T 100-mm lens to achieve a mean optical resolution of 10.4 μm/pixel. In the optical path between the cylinder and the camera, a bandpass filter (Thorlabs, $\lambda_{\text{center}} = 530$ nm, BW = 43 nm) is located to block out the LED light.

After preparation, the cylinder is placed inside the experimental chamber. The inlet pressure is fixed to 1.0 bar using PR1 while valve V1 remains closed. Valve V2 is opened to allow the experimental tank to be flushed during the flushing stage. The LED inside the chamber is turned on and 5 s later the interval timer shooting mode on the camera is activated. Fifteen seconds after camera activation, the pressure and temperature sensor data starts being recorded. Finally, 35 s after turning on the LED inside the chamber, valve V1 is opened and the system is flushed with CO_2 gas in order to fully replace the ambient air inside the tank. The time at the start of the flushing stage is $t = 0$ s and marks the start of the "experiment" stage. After flushing for 60 s, valves V1 and V2 are closed in quick succession, with the former being closed first to prevent pressurization of the experimental tank. At the end of the experiment (typically at $t = 15$ min), the experimental tank is opened and flushed using a nitrogen spray gun to prepare the experimental chamber for the next experiment.

Based on the aforementioned experimental conditions, we can calculate the relevant dimensionless numbers. Our Schmidt number is found to be $Sc = \nu/D = 515$. Since the maximum CO_2 concentration difference in the barrier is $\Delta C = C_{sat}$, we find our maximum Rayleigh number to be

$$Ra_H \equiv \frac{\beta C_{sat} g H^3}{\nu D}, \tag{1}$$

where g is the acceleration due to gravity, $\beta = (8.2 \pm 0.03)$ cm^3/mol the solutal expansion coefficient of CO_2; the saturation concentration $C_{sat} = k_H P_0$, with $k_H = (3.53 \pm 0.04) \times 10^{-4}$ mol/m^{3}Pa and $P_0 = 1.0$ bar; $D = (1.85 \pm 0.02) \times 10^{-9}$ m^2/s the diffusion coefficient of CO_2 in water; $H = 17.6 \pm 0.35$ mm the height of the liquid barrier; and $\nu = 9.5 \times 10^{-7}$ m^2/s the kinematic viscosity of water [8,30,31]. We obtain $Ra_H \approx (8.8 \pm 0.5) \times 10^6$, which is well above the critical Rayleigh number, $Ra_{H,c} = 1.29 \times 10^6$, based on the minimal aspect ratio ($\Gamma_{max} = d/H = 0.17$) of our experimental setup [32].

III. EXPERIMENTAL OBSERVATIONS

We begin by analyzing a series of liquid-air experiments, (i), (iii), and (iv) in Fig. 2, and a liquid-solid experiment, (ii) in Fig. 2. Videos of experiments (i)–(iv) can be found in the Supplemental Material [33]. Moreover, snapshots of additional experiments can be found in the Supplemental Material in Figs. S1 and S2. As the CO_2 starts dissolving into the liquid barrier, the pH of the CO_2 imbued liquid starts to decrease. Since fluorescein is a pH-sensitive fluorophore in the range $5 \lesssim pH \lesssim 10$, the emission intensity of the fluorescein dye starts to decrease, resulting in a color change of the dye from bright green to black in the images [34].

At the beginning of the experiments, $t = 0$ s, we start replacing the air atmosphere with a CO_2 atmosphere. Almost immediately, CO_2 starts dissolving into the liquid barrier, forming a CO_2-rich water layer just below the gas-liquid interface. While initially stable, the continued dissolution of CO_2 into the water barrier results in the layer becoming gravitationally unstable, as the CO_2-rich water is denser in comparison to the pure water underneath. Once this happens, a convective plume is shed from the CO_2-rich boundary layer which starts propagating downwards into the liquid barrier. In the experiments shown, the shedding of the buoyant plume occurs around $t \sim 1$ minute.

After shedding the convective plume, differences in the CO_2 front propagation dynamics can be observed. In (i) and (ii) the front appears to propagate axisymmetrically throughout the water barrier. As a result, the CO_2 front does not quite reach the lower liquid-gas, (i), or liquid-solid, (ii), interface. In contrast, the apparent axisymmetry observed in (i) and (ii) is seemingly broken in (iii) and (iv) at $t = 5$ min and $t = 12$ min, respectively. In (iv) the shedding of a lateral buoyant upwelling plume can be observed at the right side of the cylinder at the interface of the denser CO_2-rich liquid and the pure bulk liquid. In (iii), the plume appears visually centered due to the planar visualization of the 3D system. Regardless, in both cases the CO_2 front accelerates towards a higher velocity, leading to the front reaching the bottom liquid-air interface around $t \sim 10$ min in
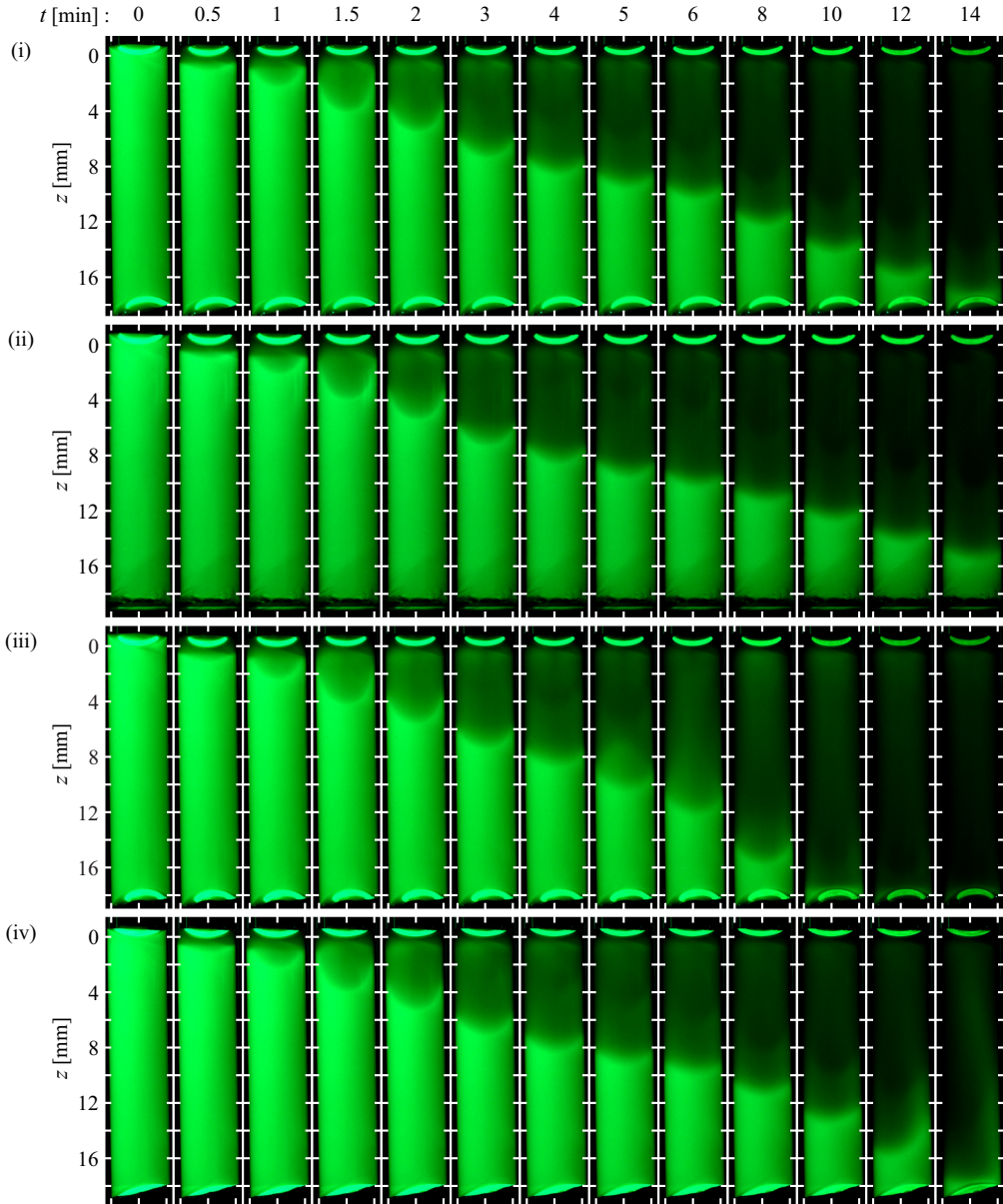
FIG. 2. Fluorescence images of the initial dissolution process of CO_2 in a vertical liquid column within a cylindrical cell. The fluorescence intensity decays with pH or increasing CO_2 concentration. At $t = 0$, the upper interface is exposed to a CO_2 gas ambient. Subsequently, a CO_2-containing layer (dark region) propagates downwards. The bottom liquid interface for (i), (iii), and (iv) is liquid-air; for (ii) it is liquid-solid. The type of boundary has no impact on the propagation dynamics of the CO_2 front. In (i) and (ii) the front propagates axisymmetrically throughout the entire water depth. In (iv), axisymmetry is broken at $t \approx 12$ min with the shedding of a lateral buoyant upwelling plume. A similar symmetry-breaking upwelling plume occurs in (iii) at $t \approx 5$ min, yet the plume appears visually centered due to the planar visualization of the 3D system. Such an event causes the front to accelerate towards a higher velocity. Coordinate z denotes the depth from the apex of the top meniscus; the horizontal ticks are 2 mm apart.
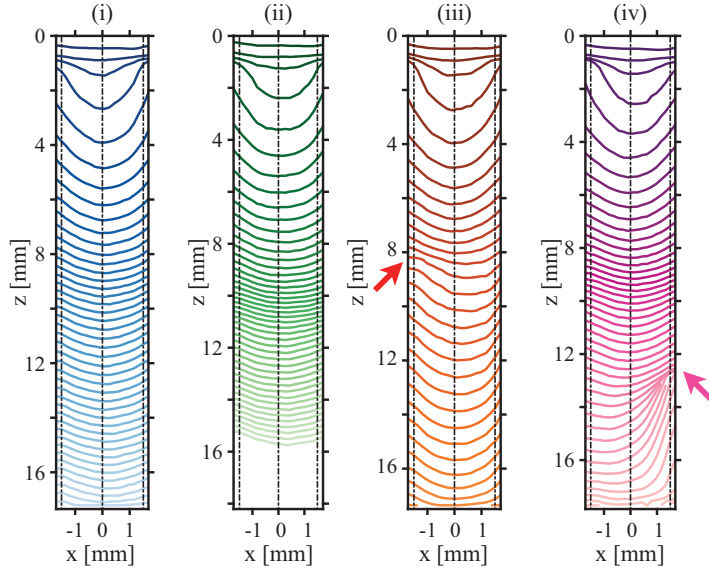
FIG. 3. (a) Propagation of the projected front surface for experiments (i)–(iv) shown in Fig. 2 during $0 < t < 15$ min. The front is defined as the isoconcentration contour $z_f = z_f(x,t)$ corresponding to a normalized intensity $I^*(x, z, t)$ value of 60%. The front is computed from the vertical intensity profiles computed across 20 equispaced positions in x. The time step between contour lines is $\Delta t = 20$ s. In (iii) and (iv), the arrows denote the front positions at which lateral plume shedding occurs, i.e., when the axisymmetric propagation is broken.

experiment (iii) and $t \sim 15$ min in experiment (iv). However, no significant amount of CO_2 exsolves from the interface, which would result in the growth of the trapped air bubble. This is expected given that in our earlier work we studied this exact system and showed that, for much shorter water barriers, bubble growth did not occur during the 15 min after the flushing stage [35]. It therefore appears that the type of bottom boundary does not affect the CO_2 propagation dynamics, but the occurrence of the shedding of a secondary plume does.

To further study the propagation dynamics, we track the progression of the CO_2 front in the liquid barrier over time. We define 20 equispaced bins along the cylinders diameter for which the vertical intensity profiles are calculated. The obtained intensity profiles are normalized with respect to the intensity profiles at $t = 0$ s in order to account for variations in illumination. The CO_2 front is defined as the isoconcentration contour $z_f = z_f(x,t)$ corresponding to a normalized intensity $I^*(x, z, t)$ value of 60%. For experiments (i)–(iv), the obtained projected front surfaces are shown in Fig. 3. The time step between the contour lines is $\Delta t = 20$ s. The front profiles of the additional experiments can be found in the Supplemental Material in Figs. S3 and S4 [33].

The shown front contours emphasize that the initial behavior for the four experiments is very similar. After the shedding of the buoyant plume by the diffusive boundary layer, the front initially rapidly accelerates and then slows down again as time progresses. As mentioned, in experiments (i) and (ii), the front reaches a stable velocity, indicated by the front contours becoming equidistant in space. For experiments (iii) and (iv), the arrows indicate the depth at which we observe the shedding of a lateral buoyant plume. After this event, the spatial distance between the lines increases again, indicating the acceleration of the front to a higher velocity. This is very similar to the initial shedding event observed from the diffusive boundary layer. The secondary plume shedding is not observed in all cases and is therefore likely related to uncontrolled noise in the experiments, such as small, local deviations in CO_2 concentration or the small inclination of the cylinder with respect to the base plate.
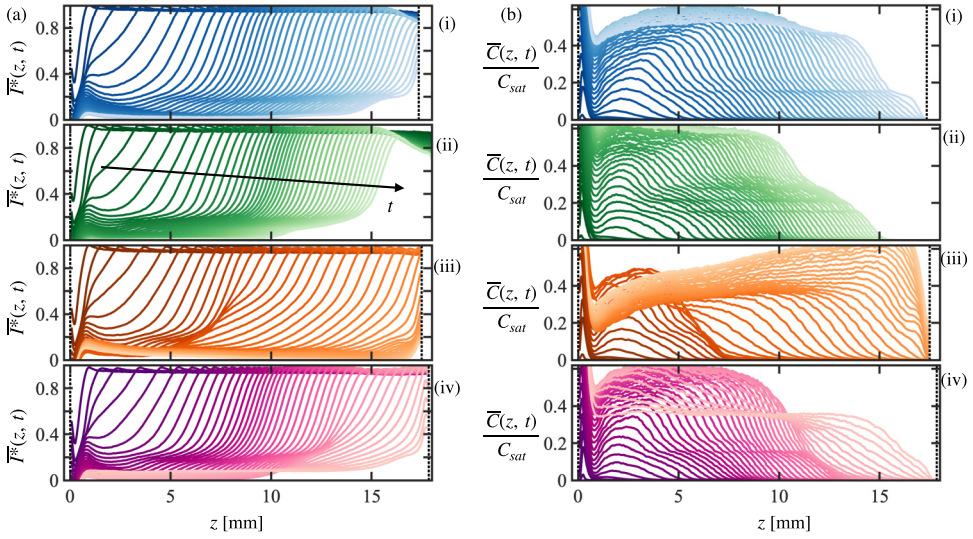
FIG. 4. (a) Normalized intensity profiles for experiments (i)–(iv) from Figs. 2 and 3. The intensity profiles have been been horizontally averaged over the entire cell diameter ($-d/2 < x < d/2$) at every depth z. The time step between consecutive profiles is $\Delta t = 20$ s for $0 < t < 15$ min. (b) Tentative concentration profiles directly obtained from $\overline{I}^*$ after calibration; C_{sat} refers to the saturation concentration. Concentration values close to the boundaries of the liquid column are tainted by the presence of a meniscus (or a solid interface) and are limited to $\overline{C}/C_{\text{sat}} < 0.6$, which corresponds to the lower bound of the pH-sensitive range of sodium fluorescein. The vertical dotted lines indicate the depth of the top ($z = 0$) and bottom boundaries of the liquid barrier.

IV. INTENSITY AND CONCENTRATION PROFILES

We continue our analysis by investigating the amount of CO_2 absorbed in the liquid barrier over time. In order to do so, we first have to obtain the intensity profiles of the fluorescein solution in the barrier and convert these to the corresponding CO_2 concentration profiles. Therefore, we start by computing the horizontally averaged intensities $G(z, t)$ which are then a function of depth z and time t only. We normalize the obtained intensities with respect to the initial intensity profile in order to account for spatial inhomogeneity of the LED lighting, defined as the normalized intensity $I = G(z, t)/G(z, 0)$. Additionally, we correct these intensity profiles for the decay in intensity due to photobleaching of the fluoroscein solution. This is achieved by measuring the decay due to photobleaching over time in a by CO_2 unaffected segment of the cylinder and correcting the measured intensities correspondingly. Finally, we once more normalize the obtained intensities by the maximum and minimum obtained intensities of the experiment which are found to be quite close for all experiments, resulting in $\overline{I}^*(z, t)$.

For experiments (i)–(iv), the obtained intensity profiles are shown in Fig. 4(a). As before, the time step between consecutive profiles is $\Delta t = 20s$ and the profiles are shown for the entire experiment, i.e., between $0 < t < 15$ min. The vertical dotted lines indicate the depth of the top ($z = 0$) and bottom boundaries of the liquid barrier. For experiments (i) and (ii), the steady propagation discussed before is clearly reflected in the intensity profiles. As the front propagates through the barrier, the intensity drops rapidly, as expected based on the snapshots from Fig. 2. Moreover, the decrease in propagation velocity is again reflected in the intensity profiles, as the spacing between the profiles decreases as time progresses. For experiments (iii) and (iv), the shedding of the lateral buoyant upwelling plume causes the intensity at certain depth to increase, resulting in overlapping intensity profiles.

As mentioned before, the emission intensity of fluorescein has a nonlinear dependency on the pH level of the liquid. Therefore, we need to obtain a calibration curve before we can convert the measured intensities to the CO_2 concentration in the barrier. To achieve this, we performed a set of experiments in which the cylinder is placed in an inverted configuration, with the top sealed and bottom open to the CO_2 atmosphere. When inverted, the CO_2-liquid mixture is stably stratified and therefore the CO_2 can only be transported up the barrier by diffusion. We obtain the intensity profiles of these experiments and use these to obtain a calibration function $C/C_{sat} = F(1 - I^*)$, linking the dimensionless concentration in the barrier to a measured intensity by means of the self-similar solution of the pure diffusion problem. A more detailed description of this process can be found in the Appendix.

Figure 4(b) shows the resulting CO_2 concentration profiles for experiments (i)–(iv). Similarly, for experiments (v)–(xii), the intensity and concentration profiles can be found in the Supplemental Material in Figs. S5 and S6 [33]. Note that we show the CO_2 concentration $\overline{C}(z, t)$ as a fraction of the saturation concentration C_{sat}, with $\overline{C}/C_{sat} < 0.6$, which corresponds to the lower bound of the pH-sensitive range of sodium fluorescein. As a result, we cannot differentiate concentration levels $\overline{C}/C_{sat} > 0.6$. The concentration values close to the boundaries of the liquid column are tainted by the presence of a meniscus (or a solid interface).

As expected, the concentration profiles of experiments (i) and (ii) show a steady progression of the CO_2 concentration in the liquid barrier. In experiments (iii) and (iv), the shedding of the lateral buoyant upwelling plume causes additional CO_2-rich liquid to be propagated downwards, while additional pure liquid is propagated upward by the plume. This is reflected by the concentration profiles, as we observe a sudden increase in concentration near the bottom of the cylinder, while the concentration decreases sharply at the top. Furthermore, an increase in mass transfer can also be observed after the shedding event, as the spatial spacing between the profile increases after shedding the buoyant plume.

Finally, we use the obtained CO_2 concentration profiles to calculate the total mass m of CO_2 absorbed by the liquid barrier as a fraction of the maximum dissolution capacity. We obtain the dissolution fraction from the CO_2 concentration profiles as

$$\frac{m(t)}{C_{sat}V} = H^{-1} \int_0^H \overline{C}(z, t)/C_{sat} \, dz, \tag{2}$$

where $m(t)$ is the total mass of CO_2 in the liquid phase, C_{sat} the saturation concentration of CO_2 in water, and $V \equiv \pi d^2 H/4$ the volume of the liquid barrier. As mentioned before, we can only measure the concentration up to $\overline{C}/C_{sat} < 0.6$, as higher concentrations are outside the pH sensitive range of the fluorescein. Figure 5 shows the obtained dissolution fraction $m(t)/(C_{sat}V)$ versus time, averaged over all 12 experiments. The wide error bars reflect the variability among experiments, such as the occurrence of the shedding of a lateral buoyant upwelling plume, and the uncertainties in the concentration calibration. Initially, the dissolution curve follows the self-similar solution for pure diffusion (dotted line), where $m = 2C_{sat}A\sqrt{Dt/\pi}$ and $A = \pi d^2/4$. However, after the onset of convection, the curve deviates, resulting in $m = 2C_{sat}A\sqrt{D_c(t - t_c)/\pi}$ (dashed line) to be the best fit, with an effective diffusion coefficient of $D_c = 30D$ and $t_c = 160$ s as the virtual time origin. Compared to other authors, who report finding $D_c/D \sim 10^2$ or 10^3 for experiments conducted in varying PVT or Hele-Shaw cells, this seems reasonable as variations in experimental conditions and cell configuration differences appear to severely affect the obtained effective diffusion coefficients [20–24].

V. FRONT PROPAGATION DYNAMICS

We carry on our analysis by focusing on the propagation dynamics of the CO_2 front in the liquid barrier. We define the position of the CO_2 front, $z_f(t)$, which we arbitrarily set to the 60%-intensity threshold of the horizontally averaged intensity profiles, $\overline{I}^*(z_f, t) = 0.6$ (cf. Fig. 4). Tracing this position in time yields Fig. 6, which shows the front trajectories of all 12 experiments versus time.
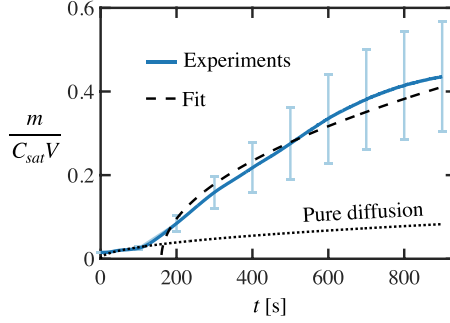
FIG. 5. Mass m of CO_2 absorbed by the liquid column as a function of time, averaged across all 12 experiments; m is normalized by the maximum dissolution capacity $C_{sat}V$, where $V \equiv \pi d^2 H/4$ is the liquid volume and C_{sat} the saturation density (or concentration) of CO_2 in water. The dissolution fraction is estimated from the 1D axial concentration profiles as $m(t)/(C_{sat}V) = H^{-1} \int_0^H \overline{C}(z, t)/C_{sat}\, dz$. The wide error bars reflect the variability between experiments and the uncertainties in concentration calibration. The dissolution curve initially follows the self-similar solution for pure diffusion (dotted line): $m = 2C_{sat}A\sqrt{Dt/\pi}$, where $A = \pi d^2/4$. At the onset of convection it starts to deviate from the purely diffusive behavior due to the contribution of convection. In that regime the curve can be described by an effective diffusive behavior $m = 2C_{sat}A\sqrt{D_c(t - t_c)/\pi}$ (dashed line), with the fit $D_c = 30D$ as the effective diffusion coefficient and $t_c = 160$ s as the virtual time origin.
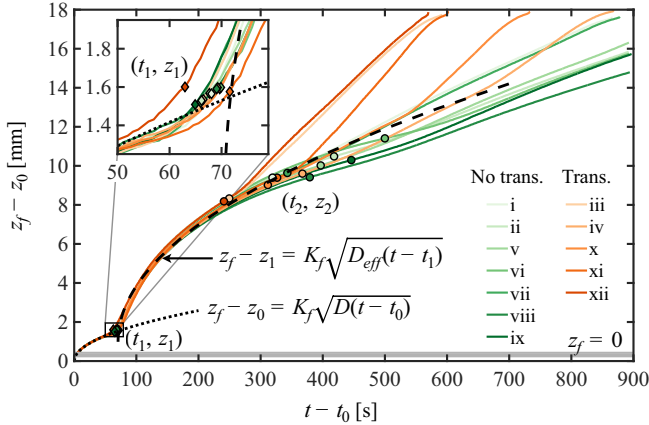
FIG. 6. Front trajectory $z_f(t)$ corresponding to the 60%-intensity threshold of the horizontally averaged intensity profiles (cf. Fig. 4), namely $\overline{I}^*(z_f, t) = 0.6$. The front trajectory of all 12 experiments is plotted, which are color coded based on the absence (greens) or the occurrence (reds) of the shedding of the upwelling plume. The time t and front position z_f (the latter defined as the distance to the apex of the top meniscus) have been offset by the (fitted) virtual origin of the diffusive regime ($t_0 = 5.5 \pm 2.2$ s and $z_0 = -0.3 \pm 0.06$ mm), which absorb the influence of the finite curvature of the top meniscus and the typical flushing response time required for full exposure to the CO_2 ambient. Initially, $z_f(t)$ follows the self-similar solution for pure diffusion (dotted line), taking $K_f \equiv 2\text{erfc}^{-1}(C_f/C_{sat}) = 4.27$ corresponding to $C_f/C_{sat} = 2.5 \times 10^{-3}$ ($I^* = 0.6$). The onset of the convective instability (diamond markers) occurs at $t = t_1$, $z_1 = z_f(t_1)$, when the front acceleration ($d^2 z_f/dt^2$) is maximum. A zoom-in is provided in the inset, which highlights the reproducibility of the time onset: $t_1 - t_0 = 67.6 \pm 2.4$ s. Thereafter, $z_f(t)$ evolves in an enhanced diffusive manner (dashed line), with an effective fitted diffusivity $D_{eff} = 8.25D$, which implies that the convective velocity of the front decays in time. At approximately $t = t_2$ (circular markers), when $d^2 z_f/dt^2 = 0$ for the first time, the front velocity stabilizes and the front propagates as expected for late stage enhanced diffusive behavior. For experiments in which a upwelling plume is shed, $t = t_2$ marks this moment and the velocity shoots off towards a higher velocity.
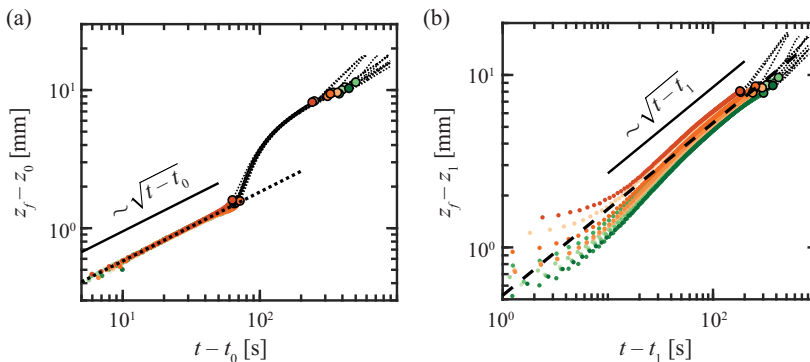
FIG. 7. Double logarithmic plot of the two distinct regimes observed for the 12 front trajectories plotted in Fig. 6: (a) the purely diffusive regime for $t < t_1$ and (b) the enhanced diffusive regime for $t_1 < t$. In (b), the convective virtual origin (t_1, z_1) is off-scale and has been fitted accordingly, given that the front behavior around t_1 is transitioning (during a transition period of ~ 10 s) and consequently does not offer a suitable virtual origin of the convective-decay regime.

The trajectories are offset by the (fitted) virtual origin $z_0 = -0.3 \pm 0.06$ mm and $t_0 = 5.5 \pm 2.2$ s of the diffusive regime. Correcting for the virtual origin absorbs the influence of the finite curvature of the top meniscus and the typical flushing response time required for full exposure to the CO_2. Furthermore, the front trajectories in Fig. 6 have been color coded based on the absence (green) or the occurrence (red) of the shedding of an upwelling plume.

As explained before, the dissolution of CO_2 into the liquid barrier results in the formation of a boundary layer at the top interface. The mass transport in this layer is driven purely by diffusion and it is therefore unsurprising that the propagation of the front $z_f(t)$ follows the self-similar solution for pure diffusion:

$$\frac{C(z, t)}{C_{\text{sat}}} = \text{erfc}\left[\frac{z - z_0}{\sqrt{4D(t - t_0)}}\right]. \tag{3}$$

The front trajectory associated to concentration C_f is thus

$$z_f - z_0 = K_f\sqrt{D(t - t_0)}, \tag{4}$$

where growth prefactor K_f depends on the concentration

$$K_f \equiv 2\text{erfc}^{-1}(C_f/C_{\text{sat}}). \tag{5}$$

In Fig. 6, the dotted line follows from Eqs. (4) and (5), taking $K_f \equiv 2\text{erfc}^{-1}(C_f/C_{\text{sat}}) = 4.27$ corresponding to $C_f/C_{\text{sat}} = 2.5 \times 10^{-3}$ ($I^* = 0.6$). We see that $z_f(t)$ follows the self-similar solution up to time t_1. We therefore define this first regime between $t_0 < t < t_1$ as the purely diffusive regime. In Fig. 7(a), we show a rescaled plot of the purely diffusive regime on a double logarithmic scale, magnifying the $z_f(t) \sim \sqrt{t - t_0}$ scaling relation.

At time t_1, we observe a sharp acceleration of the CO_2 front position, due to the onset of the convective instability. Therefore, we can find t_1 and correspondingly $z_f(t_1) = z_1$ by finding the point in time at which the front acceleration, $d^2 z_f/dt^2$, is maximum, indicated in Fig. 6 with the diamond markers. The inset shows a zoom-in around t_1 to show the reproducibility of the onset time $t_1 - t_0 = 67.6 \pm 2.4$ s, and corresponding front depth $z_1 = 1.26 \pm 0.08$ mm.

At the onset of convection, the Rayleigh number based on the thickness $\delta(t)$ of the boundary layer is given by

$$\text{Ra}_\delta(t) \equiv \frac{\beta C_{\text{sat}} g \delta^3(t)}{\nu D}. \tag{6}$$

The height of the liquid barrier H does not influence the onset. Taking the boundary layer thickness equal to the position of the front at the time we observe the onset of convection, i.e., $\delta = z_f(t_1) = z_1$, we obtain a critical value of $\text{Ra}_{z_1} = (3.30 \pm 0.6) \times 10^3$ by taking the average critical value for the 12 experiments shown in Fig. 6. We compare this value to the critical Rayleigh number from Ahlers *et al.* for Rayleigh-Bénard convection in a cylinder with adiabatic sidewalls, which we believe to be the closest available approximation to our system [32]:

$$\text{Ra}_c \equiv 1708 \left[1 + \frac{1.49}{\Gamma(t_1)^2} \right]^2, \tag{7}$$

where the local aspect ratio is defined as $\Gamma(t_1) = d/z_f(t_1)$. However, we have to emphasize the differences between our system and the systems usually described in Rayleigh-Bénard convection studies, for which (with constant Γ) Eq. (7) holds. First, in those systems, it is assumed that at the onset of convection, a linear concentration (or temperature) profile exists as the base state which subsequently becomes unstable. Second, Rayleigh-Bénard setups have reached a steady state (or are very close to such), while in our experiment the system has not and never will reach a steady state during our experimental time frame. Finally, a constant aspect ratio is assumed, while in our experiment the aspect ratio continuously decreases with time, since the front position $z_f(t)$ increases in time.

In our experiments, it is clear from Fig. 4(b) that we have nonlinear concentration profiles in the boundary layer. As a result, the thickness of the self-similar diffusion boundary layer is not easy to define. If we use δ to denote the effective thickness of the boundary layer, then $\delta = K_\delta \sqrt{D(t - t_0)}$, where the growth prefactor $K_\delta \equiv 2\text{erfc}^{-1}(C_\delta/C_{\text{sat}})$ depends on the choice of the concentration cutoff C_δ, and hence δ may differ from the depth $z_f = K_f \sqrt{D(t - t_0)}$ of our chosen isoconcentration contour $C_f/C_{\text{sat}} = 2.5 \times 10^{-3}$. For example, when we calculate Ra_c from Eq. (7), using $\Gamma(t_1) = d/z_f(t_1) \approx 2.4$, we find $\text{Ra}_c = 2.71 \times 10^3$, which is smaller than Ra_{z_1}. The value of δ that satisfies $\text{Ra}_\delta = \text{Ra}_c$, i.e., for which Eqs. (6) and (7) intersect, is exactly $\delta = \delta^* = 1.13$ mm, which is reasonably close to z_1, with a corresponding $\text{Ra}_{\delta*} = \text{Ra}_c = 2.51 \times 10^3$. This further emphasises the difficulty in defining the thickness for the self-similar diffusion boundary layer, as by selecting a lower intensity threshold, and thus higher concentration cutoff C_δ, we could have reproduced the prediction from Ahlers *et al.* [32].

In addition, we compared our findings with the work of Tan and Thorpe, who also studied the dissolution of CO_2 in water [36,37] and transient heat conduction in deep fluids [38]. In their works, they try to account for the nonlinear profile in the boundary layer within a theoretical framework which is compared with the experimental data. Using a PVT cell, they report an onset time of $t = 100$ s for CO_2 dissolution in water. Deriving an expression for the maximum transient Rayleigh number, Ra_{max}, and taking $\text{Ra}_c = 1100$ (which holds for Rayleigh-Bénard setups with a linear profile and upper free-surface [39]), yielded the transition times with close agreement with experiments [36]. When we enter the onset time obtained from our experiments, we find $\text{Ra}_{\text{max}} = 336$. This Ra_{max} is much lower than $\text{Ra}_c = 1100$, even though their setup is significantly wider than ours ($d = 90$ mm compared to our $d = 3$ mm), which suggests that our critical Rayleigh number should be even higher than 1100.

We conclude that applying the method from Refs. [36,37] to obtain the onset time leads to a severe and unrealistic overestimation for our experiments, which could be connected to the fact that in Refs. [36,37] the pressure response of the system was studied instead of directly comparing to the concentration profile. The plot reporting the onset time in Ref. [36] comes with significant uncertainty. We note that adopting $t = 64$ s instead of $t = 100$ s, which still seems consistent with the data in Ref. [36], would result in similar findings to ours. Reference [36], however, does indicate that it is quite difficult to define a precise critical Rayleigh number for experiments with a nonlinear profile, as we also discussed above. We therefore conclude that our method of finding the critical critical Rayleigh number using Eq. (6) and the boundary layer thickness at the onset gives the best

approximation of the critical Rayleigh number for the chosen isoconcentration contour, which in our case is $C_f/C_{\text{sat}} = 2.5 \times 10^{-3}$.

After the onset of convection, the front propagates seemingly in a diffusive manner, however, with an increased effective diffusion coefficient. By fitting all 12 experiments (dashed line in Fig. 6) we find that $z_f(t)$ evolves with an effective fitted diffusivity $D_{\text{eff}} = 8.25D$. For comparison, Karimaie and Lindeberg report $D_{\text{eff}} = 5.8D$ for transport of CO_2 in water confined in porous media [21]. Moreover, Fig. 7(b) shows the same regime on a double logarithmic scale, highlighting the $z_f(t) - z_1 \sim \sqrt{t - t_1}$ scaling relation. As a result, we define this regime as the enhanced diffusive regime.

Eventually, the system appears to stabilize, leading to the front propagating at a seemingly stable terminal velocity. This moment, defined as the first time at which $d^2z_f/dt^2 = 0$, is referred to as $t = t_2$, marked with circular markers in Fig. 6(b). While one could see this as a separate regime, it is in fact the late-stage behavior of the second regime. A more detailed explanation will be given in the next section. For experiments in which the shedding of an upwelling plume occurs, $t = t_2$ also happens to mark the moment at which this shoot off occurs. As mentioned before, if this event occurs, then the front accelerates and propagates with a higher velocity in comparison to the experiments in which axisymmetry is not broken. As a result, curves with a second shedding event shoot off in Fig. 6 (red curves), although their scaling behavior remains consistent with the experiments in which the shedding of the upwelling plume does not occur.

VI. NUMERICAL MODEL

A. Setup and governing equations

We continue our analysis by employing direct numerical simulations to unravel the physics governing the plume dynamics observed in the experiments. The numerical setup, shown in Fig. 1(b), is a single-phase buoyancy-driven flow confined in a cylinder with an adiabatic sidewall and free-shear surfaces at top and bottom. The system is subjected to constant saturation concentration of carbon dioxide at the upper plate and zero concentration at the bottom, in order to mimic the liquid-gas system. By varying the domain height numerically, we confirmed the independence of the propagation dynamics on the bottom boundary conditions. The dimensionless form of the advection-diffusion equation coupled with the three-dimensional Navier-Stokes equations are employed under the incomprehensibility condition and the Oberbeck-Boussinesq approximation [in order to account for buoyancy forces caused by the (small) density variations],

$$\frac{\partial \tilde{C}}{\partial \tilde{t}} + \tilde{\mathbf{u}} \cdot \nabla \tilde{C} = \frac{1}{\sqrt{\text{RaSc}}} \nabla^2 \tilde{C}, \tag{8a}$$

$$\frac{\partial \tilde{\mathbf{u}}}{\partial \tilde{t}} + \tilde{\mathbf{u}} \cdot \nabla \tilde{\mathbf{u}} = -\nabla \tilde{P} + \sqrt{\frac{\text{Sc}}{\text{Ra}}} \nabla^2 \tilde{\mathbf{u}} + \tilde{C}\hat{\mathbf{e}}_{\mathbf{g}} \cdot \hat{\mathbf{e}}_k, \tag{8b}$$

$$\nabla \cdot \tilde{\mathbf{u}} = 0. \tag{8c}$$

Here $\tilde{C}$, $\tilde{\mathbf{u}}$, and $\tilde{P}$ denote the dimensionless concentration, velocity, and pressure, respectively. The height of the cylinder H, the carbon dioxide saturation concentration C_s, and the free fall velocity $\sqrt{g\beta C_s H}$ have been used for normalization of the equations, where g is the gravitational acceleration and β the (isobaric and isothermal) volumetric concentration expansion coefficient. ∇ is the gradient operator in cylindrical coordinates, $\hat{\mathbf{e}}_{\mathbf{g}}$ is the unit normal vector in direction of the gravitational acceleration, and $\hat{\mathbf{e}}_k (k = z, r, \theta)$ are the unit normal vectors pointing toward the axial, radial, or azimuthal directions as shown in Fig. 1(c). The control parameters of the numerical model are the Rayleigh number Ra_H and the Schmidt number Sc as defined in Sec. III.

The governing equations (8) have been solved using a second-order accurate finite-difference scheme on a staggered grid and a fractional-step time-marching approach, the detail of which can be found in Ref. [40]. Introducing a disturbance to the system is necessary to trigger the instabilities arising from the buoyancy-driven convection. Hence, three different sources of disturbance are
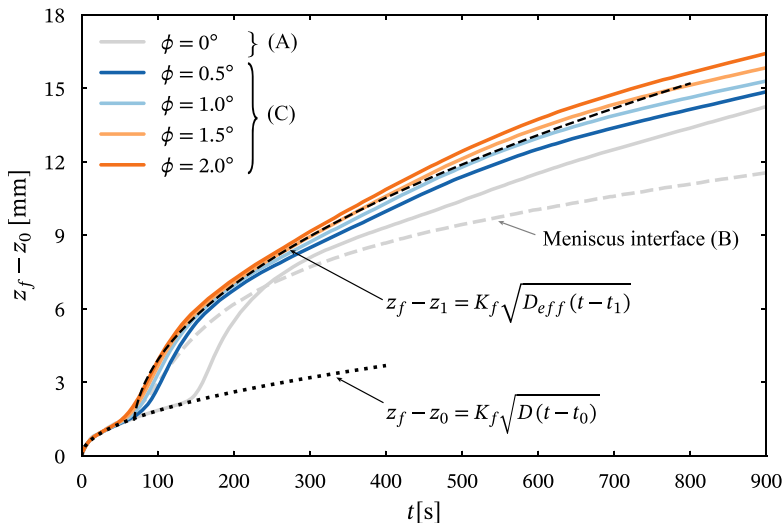
FIG. 8. Front trajectory $z_f(t)$ corresponding to $\overline{C}(z)/C_{\text{sat}} = 2.5 \times 10^{-3}$ obtained via numerical simulations performed under different conditions, namely cases (A)–(C) as explained in the main text. The analytical solution of the purely diffusive problem (dotted black line) and the experimentally averaged trajectory after the onset of convection (dashed black line) have been provided for comparison.

tested in the numerical simulations in order to find the most appropriate setup which reasonably replicates the experimental observation. These are

(A) a perturbed initial concentration field with a random positive noise throughout the system, whose amplitude varies between zero and 1% of the carbon dioxide saturation concentration;

(B) a meniscus liquid-gas interface at the top rather than a flat interfacial boundary. The meniscus shape was approximated by a cosine profile with a maximum depth of $0.01H$ at the center of the domain. Saturation concentration and no-slip velocity conditions are enforced at the interface using an immersed boundary method based on linear interpolations as developed in Ref. [41];

(C) a slight tilt of the container relative to the direction of gravity, see Fig. 1(c). The tilting has been performed by rotating the gravitational acceleration vector **g** by the angle of ϕ with respect to the negative axial direction in $\theta = 0$ plane. The inclination angles of $\phi = 0.5°$, $1°$, $1.5°$, and $2°$ have been tested in the numerical simulations.

Simulations have been conducted for the aforementioned cases (A)–(C) with different sources of disturbance. The grid resolution of $32 \times 192 \times 256$ in radial, azimuthal, and axial directions, respectively, similarly to that of confined-rotating Rayleigh-Bénard convection [42], has been used after a grid independence check has been performed. Time marching has been achieved with variable times steps with a maximum of $d\tilde{t} = 2 \times 10^{-3}$ and CFL $= 5 \times 10^{-1}$. The input of the simulations are the aspect ratio of the setup $\Gamma = d/H$, the height-based Rayleigh number Ra_H, and the Schmidt number Sc which have been chosen as 0.1704, 8.8×10^6, and 515, in accordance with the experiments.

B. Numerical results

The vertical location of the front corresponding to $\overline{C}(z)/C_{\text{sat}} = 2.5 \times 10^{-3}$, consistent with the analysis of the experimental results, has been plotted as a function of time in Fig. 8 and compared to the experiments. The front location follows that of the pure diffusion problem in all cases up to the moment when convection sets in. Looking into the transition time, a remarkable discrepancy exists between the experiments and case (A) where the initial concentration field is perturbed. On the other hand, the agreement is reasonable for cases (B) and (C). For case (B), in which the top interface is
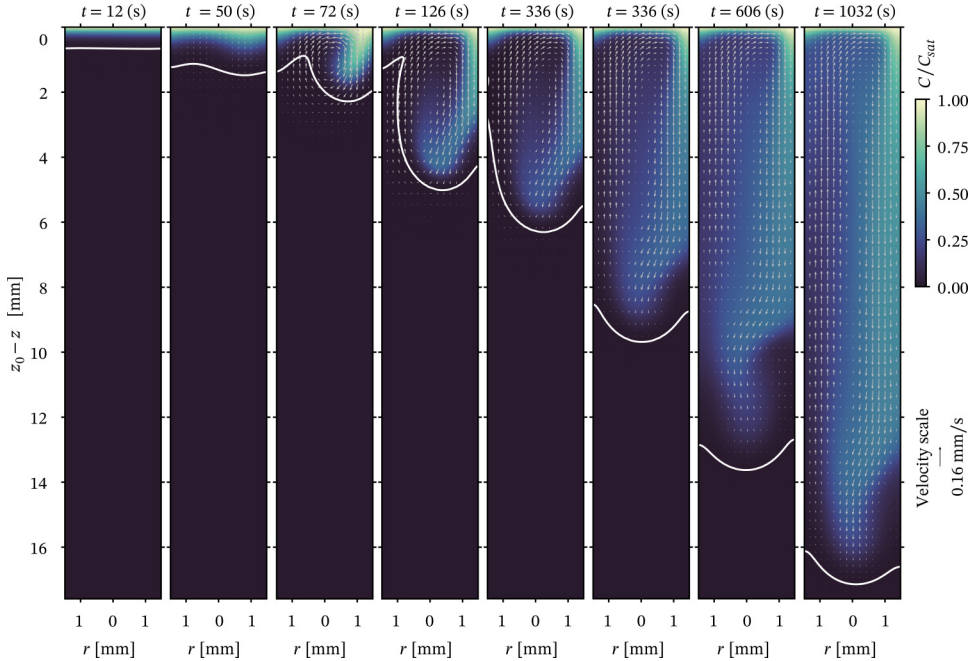
FIG. 9. Time evolution of carbon dioxide concentration obtained by numerical simulations for case (C) with inclination angle of $\phi = 1.5°$. The setup has been tilted in the $\theta = 0°$ plane from which the snapshots have been taken. The white contour lines show the front profile associated with $C_f/C_{\text{sat}} = 2.5 \times 10^{-3}$. Vectors denote the velocity field, the scaling of which has been provided in the figure.

modelled as a meniscus, it can be seen that, despite an accurate prediction of the onset time, the front velocity after the onset of convection is underestimated. Only the simulations from case (C), in which the setup is tilted and the shedding of the plume is therefore asymmetric, can reproduce the transient front location obtained in the experiments reasonably well. On this basis, we conclude that the dynamics are very sensitive to small tilt angles and that likely such a small misalignment also exists in the present experiments. Accordingly, we continue by analyzing the results obtained by numerical modeling for case (C), specifically with an inclination angle of $\phi = 1.5°$, which shows the best agreement with the experiments. For reference, the carbon dioxide concentration profile for case (B) with the meniscus interface can be found in the Supplemental Material [33].

Figure 9 shows the simulation snapshots for the carbon dioxide concentration profile superimposed with the front isocontour corresponding to $C_f/C_{\text{sat}} = 2.5 \times 10^{-3}$ and vectors representing the velocity field. The shown slices correspond to the inclination plane $\theta = 0$, the plane in which also the gravity vector is tilted. Initially, the front isocontour propagates as a horizontal line, following the analytical solution of the pure diffusion problem as shown in Fig. 8. Around $t \sim 1$ minute, as observed in Fig. 8, convection sets in and as a result a vortex forms above the front whose direction is clockwise and consistent with the tilting direction of the setup. Therefore, the front shape gets distorted complying with the flow structure forming behind. The generated convective flow remains active behind the front during its entire evolution from top to the lower boundary of the setup and its deformed shape at very low concentrations suggests a complex concentration field in the solution. Remarkable asymmetry in the front profile, particularly at the transition time, is observed from the simulations result as opposed to the experimental measurements. However, this also strongly depends on the angle of the view. The shape evolution of the front isocontour, shown in Fig. 10 for two different two-dimensional slices corresponding to $\theta = 0°$ and $\theta = 90°$, indicates axisymmetric or asymmetric profiles depending on the frame of reference chosen. The 3D shape of the front
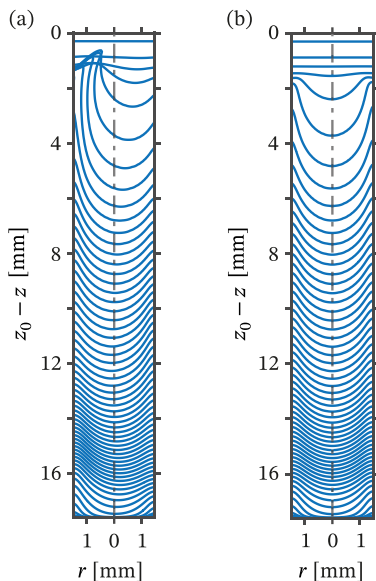
FIG. 10. Propagation of the front isosurface obtained from numerical simulations for case (C) with inclination angle of $\phi = 1.5°$. The front isosurfaces correspond to $C_f/C_{sat} = 2.5 \times 10^{-3}$ and have been taken at (a) $\theta = 0$, i.e., the inclination plane of gravity and (b) $\theta = 90°$ plane. Note that the propagation appears to be axisymmetric in the latter.

isosurface has also been plotted in time in Fig. 12, which will be discussed in more detail in the next section in order to clarify the physical mechanisms governing the interface dynamics.

C. Front local propagation velocity

Next, we consider the propagation of the front in more detail. As shown schematically in Fig. 11, the velocity ($\mathbf{u}_{iso}$) of an interface element dA of the front can be decomposed into a component due to the advection of the underlying fluid element and a propagation relative to the latter ($\mathbf{V}$), such that $\mathbf{u}_{iso} = \mathbf{u}_f + \mathbf{V}$. By definition, the interface propagation is normal to the isosurface such that $\mathbf{V} = v_n\hat{\mathbf{n}}$, with the surface unit normal vector $\hat{\mathbf{n}} = \nabla C/|\nabla C|$. Following an approach previously employed for enstrophy isosurfaces in turbulent flows [43,44], isoscalar surfaces in turbulent scalar mixing with chemical reactions [45], and flame propagation in combustion problems [46], we can derive an expression for the interface propagation velocity v_n by noting that in a frame of reference moving with the isosurface element, the total rate of change of concentration is zero. This leads to

$$\frac{D^s C}{D^s t} = \frac{\partial C}{\partial t} + \mathbf{u}_{iso} \cdot \nabla C = \frac{\partial C}{\partial t} + (v_n\hat{\mathbf{n}} + \mathbf{u}_f) \cdot \nabla C = 0, \tag{9}$$
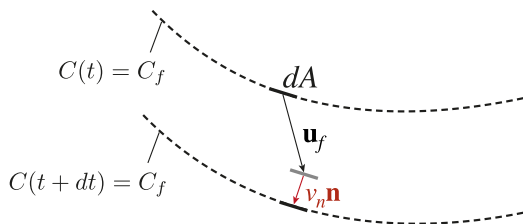
FIG. 11. Graphical representation of the local propagation velocity of the front isosurface.
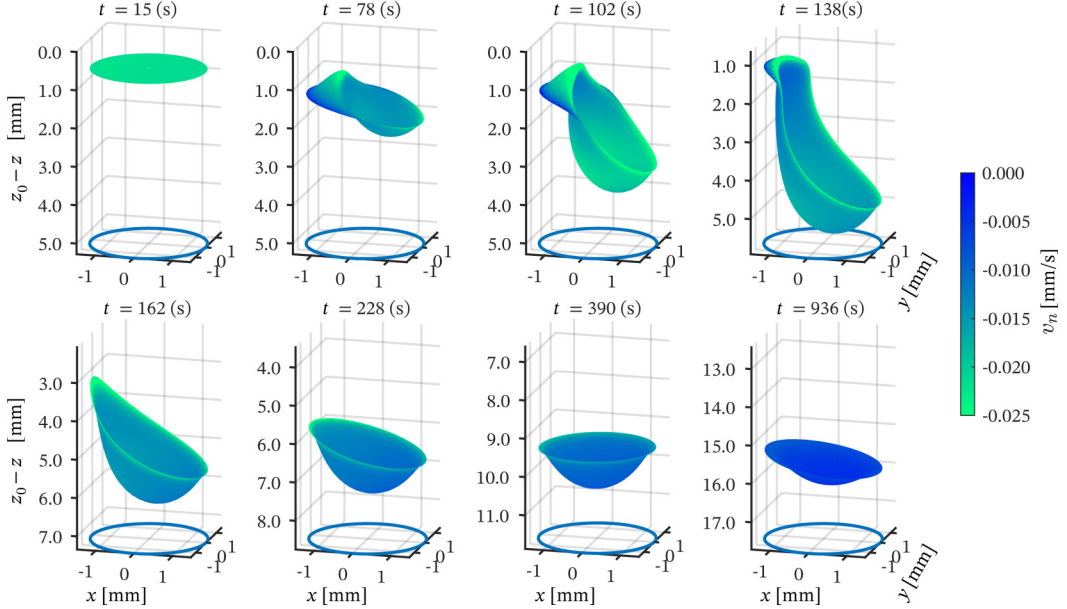
FIG. 12. Three-dimensional plot of the front isosurface evolving in time for case (C) with inclination angle of $\phi = 1.5°$. The isosurfaces correspond to $C_f/C_{\text{sat}} = 2.5 \times 10^{-3}$. The color map indicates the local propagation velocity of the front v_n normal to the isosurface calculated according to Eq. (10).

which can be solved for v_n to yield

$$v_n = -\frac{\frac{\partial C}{\partial t} + \mathbf{u}_f \cdot \nabla C}{|\nabla C|} = -\frac{\frac{DC}{Dt}}{|\nabla C|} = -\frac{D\nabla^2 C}{|\nabla C|}. \tag{10}$$

Given the incompressibility of the fluid, advection does not affect the mean interface position. The front propagation is therefore solely related to v_n and therefore diffusive in nature at all times. A quantitative relation can be obtained by equating the volume flux across the convoluted interface to that through the mean interface according to [47,48]

$$Q \equiv \int_{A_{\text{iso}}} v_n dA = A_0 \frac{dz_m}{dt}, \tag{11}$$

where the integration is over the surface area A_{iso} of the isocontour. Using an average of v_n across A_{iso} denoted by the overbar, this leads to

$$\frac{dz_m}{dt} = \frac{A_{\text{iso}}}{A_0} \bar{v}_n, \tag{12}$$

which now expresses the mean front propagation as diffusive propagation ($\bar{v}_n$) amplified by interface convolutions. Note that here we use z_m to denote the mean position of the isosurface instead of z_f in order to distinguish the volume average implied by Eq. (11) from the 2D average used for z_f.

Figure 12 shows the front corresponding to the isosurface at $C/C_{\text{sat}} = 2.5 \times 10^{-3}$ at different moments in time and color coded with the local magnitude of v_n. From these snapshots it becomes clear how convection significantly enhances the interfacial surface area, which is then decreased again as a result of the interface propagation. Convection is also seen to increase v_n locally, in particular around $t = 100s$, which is due to a steepening of the scalar gradients close to the front (see also Fig. 9). Here it should be noted that $\hat{\mathbf{n}} = \nabla C / |\nabla C|$ always points toward the region with
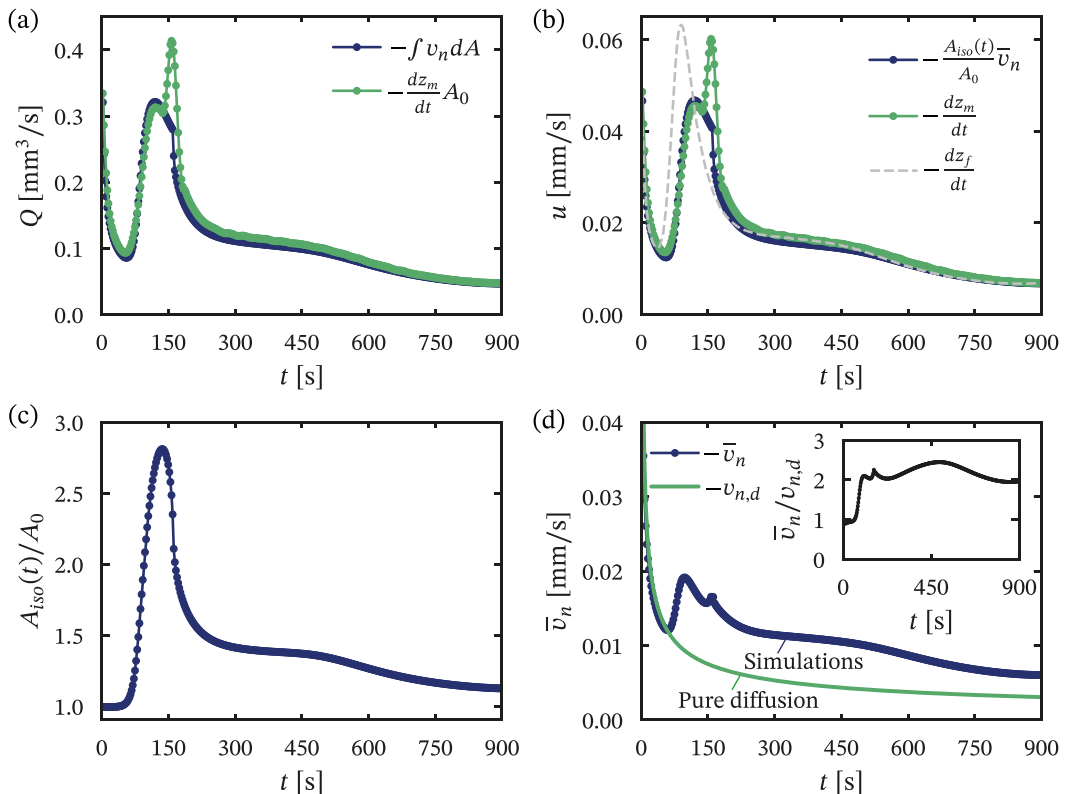
FIG. 13. (a) Volumetric flux Q of the local propagation velocity v_n across the front isosurface, compared to the rate of change in the mean volume above the isosurface, $A_0 dz_m/dt$. (b) Front propagation velocity computed from the time evolution of the cross-sectional average of the 3D isosurface, dz_m/dt, and from the product of the relative surface area and averaged local propagation velocity. dz_f/dt is provided where z_f is the front trajectory obtained from the horizontally averaged concentration profile in 2D slices, in accordance with the front tracking approach in experiments. (c) Relative surface area of the isosurface with respect to the cross sectional area of the cylinder, A_0. (d) Temporal evolution of the averaged local propagation velocity, $\overline{v}_n$, of the isosurface, compared to the pure diffusive case, $v_{n,d}$, where it equals the front propagation velocity $dz_m/dt = K_f[D(t - t_0)]^{-1/2}$, with K_f defined in Eq. (5). The ratio $\overline{v}_n/v_{n,d}$, is shown in the inset.

higher concentrations, i.e., the region above the front isosurface, such that negative values of v_n correspond to an outward propagation of the interface.

Results for computing the volume flux across the interface from integrating v_n (Q) and based on evaluating $A_0 dz_m/dt$ are compared in Fig. 13(a). As can be seen the agreement is very good as expected, apart from a short period around $t \approx 150$ s. During this time, the wall-parallel part of the isosurface reaches the wall (see Fig. 12), leading to a sudden decrease in the front surface area as well as in its mean location, which is not captured sufficiently accurately by our method to extract the isosurface.

The panel in Fig. 13(b) presents the same data as Fig. 13(a), only this time expressed as effective mean front velocities according to (12). This form enables a direct comparison to the front velocity based on z_f, previously shown in Fig. 8. For most times the agreement between dz_f/dt and dz_m/dt is good, but a significant difference arises for the peak following the onset of convection. This highlights that especially during this period ($70 \lesssim t \lesssim 200$) it is important to account for the three-dimensionality of the flow.

The volumetric fluxes and propagation velocity of the front are similarly calculated for the simulations in case (B), where the top boundary is modelled with the meniscus interface, and are compared in Figs. S8(a) and S8(b) in the Supplemental Material [33]. The agreement at the times when the isosurface attains its maximum surface area is better for that case, due to less interaction of the isosurface with the wall (see Fig. S7 in the Supplemental Material [33]).

For a closer analysis we disentangle the effects leading to diffusion enhancement, followed by faster propagation of the front after transition to convection. Equation (12) encompasses the two key parameters contributing to the front dynamics; the relative area of the isosurface, A_{iso}/A_0, multiplied by the averaged local propagation velocity, $\overline{v}_n$, which together define the rate of diffusive transport across the front interface. Any changes in the front surface area or the concentration gradients (diffusive fluxes) in its vicinity can ultimately alter the diffusion rate across the front isosurface and impact the propagation velocity. Therefore, we plot the time evolution of A_{iso}/A_0 and $\overline{v}_n$ in Figs. 13(c) and 13(d), respectively. The front velocity in the pure diffusion problem, which is solely equivalent to $\overline{v}_n$ [the front remains always flat and thus the relative surface area is unity in Eq. (12)], has analytically been obtained from Eq. (4) as $v_{n,d} = K_f D(t - t_0)^{-1/2}$ and plotted in Fig. 13(d). The relative local propagation velocity of the front with respect to that of the pure diffusion problem, i.e., $\overline{v}_n/v_{n,d}$, is also shown in the inset.

Up to transition time, the front isosurface remains flat, meaning that the relative surface area does not change in this period and thus remains equal to unity. Similarly, the local propagation velocity follows that of the pure diffusion problem as they are essentially the same before the onset of convection, which leads to a relative local propagation velocity equal to unity, as indicated in the inset. The value of $\overline{v}_n$ decreases within this period, complying to the front dynamics governed by diffusion regime, i.e., $dz_m/dt \sim t^{-1/2}$.

Once convection sets in, the underlying flow field distorts the front intensely, as demonstrated in Figs. 9 and 12 around $t \approx 1$ min. This leads to a significant increase in the surface area of the front, see Fig. 13(c), as well as the adjacent concentration gradients, ∇C. The latter is reflected in local propagation velocity when it increases after $t \approx 1$ min in Fig. 13(d) ($\overline{v}_n \sim \nabla^2 C$ and $\nabla^2 C$ is higher in the vicinity of a stretched interface since ∇C has nonzero components in lateral directions). Shown in the inset is that the onset of convection effectively doubles the relative propagation velocity. As a result, lateral diffusive fluxes across the interface intensify, which act against the further convolution of the front and lead to a reflattening process, once a maximum surface area is reached. Consequently, the front surface area and local propagation velocity drop after the maximum distortion until a "steady state" is reached [Figs. 13(c) and 13(d)]. They determine the trend of the total propagation velocity shown in Fig. 13(b). At this point, the advective fluxes causing the front distortion approximately equal the lateral diffusive fluxes across the interface which leads to much lower temporal variations afterwards.

The equilibrium state is even more evident in the simulations for case (B), with the meniscus interface at the top boundary. In these simulations, the distortion of the front is less pronounced and therefore the front interface has enough time to almost completely go through the reflattening process, as shown in Fig. S7 at $t = 1737$ s. Moreover, the relative front surface area and local propagation velocity, depicted in Figs. S8(c) and S8(d), approach the values close to unity, meaning that the dynamics pertinent to the pure-diffusion regime are almost recovered and the front interface propagates with a nearly constant velocity at late times.

Therefore, although the emerged flow field after the onset of convection does not directly impact the mean location of the front, it does play a significant role in amplifying the carbon dioxide diffusion rate across the front interface through increasing the front interface surface area and local concentration gradients. The front isosurface accelerates remarkably after the onset of convection and the front trajectory after the onset can still be described approximately with a relation similar to the analytical solution of a pure-diffusion problem as described in Eq. (4), albeit with an effective diffusion constant D_{eff}, which accounts for the enhanced diffusion observed in the convective regime. For the case specifically studied here, the post-transition front trajectory, namely

the enhanced diffusive regime, can be approximated with $D_{eff} = 8.25D$, plotted for comparison with the data obtained via experiments and numerical simulations in Figs. 6 and 8, respectively.

VII. CONCLUSIONS

We have investigated the dissolution and subsequent propagation dynamics of carbon dioxide gas into a liquid barrier confined to a vertical glass cylinder, both experimentally and through direct numerical simulations. Replacing the ambient air above the cylinder with a CO_2 atmosphere, induces the dissolution of CO_2 into the liquid barrier. Initially, the dissolution of CO_2 results in the formation of a CO_2-rich water layer, which is denser in comparison to pure water, at the top gas-liquid interface. While initially stable, continued dissolution of CO_2 into the water barrier results in the layer becoming gravitationally unstable, leading to the onset of buoyancy-driven convection and, consequently, the shedding of a buoyant plume. By adding sodium fluorescein, a pH-sensitive fluorophore, we directly visualize the dissolution and propagation of the CO_2 across the liquid barrier. Tracking the CO_2 front propagation in time allows us to define two clear propagation regimes.

At first, before the onset of convection, the growth dynamics of the boundary layer are purely governed by diffusion (the diffusive regime). The Rayleigh number continues to increase until it reaches the critical value of our system of $Ra_{z_1} = (3.30 \pm 0.6) \times 10^3$ and convection starts. After the onset of convection, the propagation dynamics of the CO_2 front appear to also behave diffusively, albeit with an effective diffusion coefficient 8.5 times larger than expected for CO_2 in water. This enhanced diffusive regime remains throughout the experiments, until the system either reaches a "steady state," at which point the front propagates at a constant velocity until it reaches the bottom interface, or becomes unstable, leading to the shedding of an upwelling plume and accelerating towards a higher velocity.

Using direct numerical simulations, we have uncovered the roots of the observed propagation mechanics. Initially, before the onset of convection, the simulations show that the relative surface area of the CO_2 front does not increase and the local propagation velocity follows the expected trend for a purely diffusive problem. After the onset of convection, first the relative surface area and local concentration gradients incorporated in the averaged local propagation velocity on the front, $\bar{v}_n$, concurrently increase due to the emerging local fluid flow. The diffusive transport rate across the front interface is remarkably amplified, leading to much faster propagation velocity of the CO_2 front. In the meantime, increased lateral diffusive fluxes across the distorted interface act as a competing mechanism against the advective fluxes and further convolution of the front. This triggers the reflattening process of the CO_2 front as a result of which the front surface area and local propagation velocity drop and a "steady state" is reached. At this point, the advective effects causing the front distortion approximately equal the diffusive flattening of the interface, resulting in the front propagating at a seemingly constant velocity. The front trajectory after the onset can still be described with a relation similar to the analytical solution of a pure-diffusion problem, albeit with an effective diffusion 8.5 times higher than expected for CO_2 in water.

Our findings offer insight into the mass-transfer effects encountered in laterally confined CO_2 sequestration operations, as well as microfluidic or microreactor devices comprising segmented gas-liquid systems or density-changing solutes. Such a better understanding of the formation and propagation dynamics of the convective plume can uncover previously undiscovered mechanics pertaining to the dissolution and mixing off chemical species in a variety of applications. An interesting and relevant route to follow is the extension of our work to vessels with larger lateral extension (larger aspect ratio), where many plumes drive the downwards transport of the flow. Based on the results of Shishkina [49], we expect a strong increase of the transport with increasing aspect ratio. For very large aspect ratios, the unconfined limit of CO_2 sequestration will be approximated [6].

APPENDIX: INTENSITY PROFILE NORMALIZATION AND CONCENTRATION CALIBRATION

The grayvalue (green channel value) profile $G(z, t)$ of the raw fluorescence images is first normalized by the initial profile, i.e., without significant amounts of CO_2 present in the liquid, to correct for the spatial inhomogeneity of the LED lighting. Thus, $I = G(z, t)/G(z, 0)$ is the normalized apparent intensity. However, I decays exponentially in time due to photobleaching. We assume that rate of change of the I is the sum of the rate of change due to CO_2 quenching (pH change) and the rate of change imposed by photobleaching:

$$\frac{dI}{dt} = \frac{d\hat{I}}{dt} - \beta\hat{I}, \tag{A1}$$

where $\hat{I}$ denotes the true intensity (corrected for photobleaching) and β is the photobleaching rate constant. It follows that β is in fact pH dependent, i.e., $\beta = \beta(\hat{I}^*)$. We approximate the dependence to be linear as $\beta = a\hat{I} + b$, where coefficients a and b are obtained experimentally, e.g., from the intensity decay rate within the CO_2-free region in the water column in combination with measurements from purely diffusive experiments (where the cell is inverted). We find $a = -5.0 \pm 0.2 \times 10^{-4}\,\text{s}^{-1}$ and $b = 6.8 \pm 0.3 \times 10^{-4}\,\text{s}^{-1}$ across the 12 experiments. The corrected
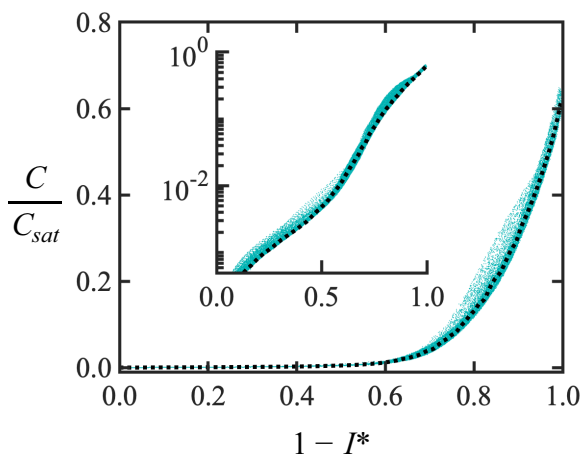
FIG. 14. Calibration curve (dotted line), which relates the normalized intensity I^* to the dimensionless concentration, C/C_{sat} under our particular experimental conditions. The blue data points are measurements of the self-similar intensity profile $I^*(\eta)$ of the calibration (pure diffusion) experiment, for which $C(\eta)/C_{\text{sat}} = \text{erfc}(\eta)$. Inset: Same calibration curve plotted in semi-logarithmic axes.

intensity at any location z can be solved for iteratively by linearising Eq. (A1) as follows:

$$\hat{I}(z)_{n+1} - \hat{I}(z)_n = I_{n+1}(z) - I_n(z) + \beta_n(z)\hat{I}_n(z)\Delta t, \tag{A2}$$

where subscript n refers to the current time step or image frame and Δt is the time difference between consecutive time steps. Finally, the corrected intensity is then renormalized by the maximum and minimum intensity values (within the central region far from the shadowing effect of the meniscii or solid boundaries). Thus,

$$I^*(z,\ t) = \frac{\hat{I}(z,\ t) - \min(\hat{I})}{\max(\hat{I}) - \min(\hat{I})}, \tag{A3}$$

keeping in mind that $\max(\hat{I}) \approx 1.0$ and $\min(\hat{I}) \approx 0.4$ are quite close (ideally identical) for all experiments.

For the concentration calibration, we relate the intensity profile of a diffusive experiment to the self-similar profile $C/C_{\text{sat}} = \text{erfc}(\eta)$, with $\eta = z/\sqrt{4Dt}$. Consequently, the intensity profiles evolves self-similarly, too: $I^*(z,\ t)$ collapse into the same curve $I^*(\eta)$. Thus, the calibration function $C/C_{\text{sat}} = F(1 - I^*)$ can be obtained by a monotonic fit on a plot of $\text{erfc}(\eta)$ vs $1 - I^*(\eta)$, which is provided in Fig. 14.

---

[1] Y. Cao, C. Soares, N. Padoin, and T. Noël, Gas bubbles have controversial effects on Taylor flow electrochemistry, Chem. Eng. J. **406**, 126811 (2021).

[2] I. Bagemihl, C. Bhatraju, J. R. Van Ommen, and V. Van Steijn, Electrochemical reduction of CO_2 in tubular flow cells under gas–liquid taylor flow, ACS Sust. Chem. Eng. **10**, 12580 (2022).

[3] M. Abolhasani, A. Günther, and E. Kumacheva, Microfluidic studies of carbon dioxide, Angew. Chem. Int. Ed. **53**, 7992 (2014).

[4] H. Hassanzadeh, M. Pooladi-Darvish, and D. W. Keith, Scaling behavior of convective mixing, with application to geological storage of CO_2, AIChE J. **53**, 1121 (2007).

[5] H. Emami-Meybodi, H. Hassanzadeh, C. P. Green, and J. Ennis-King, Convective dissolution of CO_2 in saline aquifers: Progress in modeling and experiments, Int. J. Greenhouse Gas Contr. **40**, 238 (2015).

[6] M. De Paoli, Influence of reservoir properties on the dynamics of a migrating current of carbon dioxide, Phys. Fluids **33**, 016602 (2021).

[7] S. Backhaus, K. Turitsyn, and R. E. Ecke, Convective Instability and Mass Transport of Diffusion Layers in a Hele-Shaw Geometry, Phys. Rev. Lett. **106**, 104501 (2011).

[8] V. Loodts, L. Rongy, and A. De Wit, Impact of pressure, salt concentration, and temperature on the convective dissolution of carbon dioxide in aqueous solutions, Chaos **24**, 043120 (2014).

[9] M. C. Rogers and S. W. Morris, Buoyant Plumes and Vortex Rings in an Autocatalytic Chemical Reaction, Phys. Rev. Lett. **95**, 024505 (2005).

[10] V. Loodts, H. Saghou, B. Knaepen, L. Rongy, and A. De Wit, Differential diffusivity effects in reactive convective dissolution, Fluids **3**, 83 (2018).

[11] Y. Gu, V. Hegde, and K. J. Bishop, Measurement and mitigation of free convection in microfluidic gradient generators, Lab Chip **18**, 3371 (2018).

[12] F. Sepahi, N. Pande, K. L. Chong, G. Mul, R. Verzicco, D. Lohse, B. T. Mei, and D. Krug, The effect of buoyancy driven convection on the growth and dissolution of bubbles on electrodes, Electrochim. Acta **403**, 139616 (2022).

[13] E. Dietrich, S. Wildeman, C. W. Visser, K. Hofhuis, E. S. Kooij, H. J. W. Zandvliet, and D. Lohse, Role of natural convection in the dissolution of sessile droplets, J. Fluid Mech. **794**, 45 (2016).

[14] K. L. Chong, Y. Li, C. S. Ng, R. Verzicco, and D. Lohse, Convection-dominated dissolution for single and multiple immersed sessile droplets, J. Fluid Mech. **892**, A21 (2020).

[15] O. R. Enríquez, C. Sun, D. Lohse, A. Prosperetti, and D. Van Der Meer, The quasi-static growth of CO_2 bubbles, J. Fluid Mech. **741**, R1 (2014).

[16] Á. Moreno Soto, O. R. Enríquez, A. Prosperetti, D. Lohse, and D. van der Meer, Transition to convection in single bubble diffusive growth, J. Fluid Mech. **871**, 332 (2019).

[17] R. N. Moghaddam, B. Rostami, P. Pourafshary, and Y. Fallahzadeh, Quantification of density-driven natural convection for dissolution mechanism in CO_2 sequestration, Transp. Porous Media **92**, 439 (2012).

[18] Y. Gholami, R. Azin, R. Fatehi, S. Osfouri, and A. Bahadori, Prediction of carbon dioxide dissolution in bulk water under isothermal pressure decay at different boundary conditions, J. Mol. Liq. **202**, 23 (2015).

[19] Y. Tang, Z. Li, R. Wang, M. Cui, X. Wang, Z. Lun, and Y. Lu, Experimental study on the density-driven carbon dioxide convective diffusion in formation water at reservoir conditions, ACS Omega **4**, 11082 (2019).

[20] F. Du, H. Ma, and Y. Gu, Three different periods of CO_2 dissolution into a light crude oil, Can. J. Chem. Eng. **97**, 330 (2019).

[21] H. Karimaie and E. Lindeberg, Experimental verification of CO_2 dissolution rate due to diffusion induced convection, Energy Proc. **114**, 4917 (2017).

[22] R. Farajzadeh, P. L. Zitha, and J. Bruining, Enhanced mass transfer of CO_2 into water: Experiment and modeling, Ind. Eng. Chem. Res. **48**, 6423 (2009).

[23] P. Yang, H. Guo, Z. Wang, and Q. Zhou, Density and volumetric properties of binary mixtures of CO_2+ hexadecane from (303.2 to 473.2) K and pressures up to 50.0 MPa, J. Chem. Eng. Data **64**, 2568 (2019).

[24] R. Zhao, M. Xu, J. Yang, J. Y. Fu, M. Heng, and X.-a. Yue, Non-constant diffusion behavior for CO_2 diffusion into brine: Influence of density-driven convection, J. Solution Chem. **47**, 1926 (2018).

[25] M. J. Doughty, ph dependent spectral properties of sodium fluorescein ophthalmic solutions revisited, Ophthal. Physiol. Opt. **30**, 167 (2010).

[26] T. A. Robertson, F. Bunel, and M. S. Roberts, Fluorescein derivatives in intravital fluorescence imaging, Cells **2**, 591 (2013).

[27] S. Yewalkar, T. Wu, D. Kuan, H. Wang, D. Li, A. Johnson, D. Posarac, S. Duff, and X. T. Bi, Applicability of differential fluorescein diacetate and propidium iodide fluorescence staining for monitoring algal growth and viability, Waste Disposal Sust. Energy **1**, 199 (2019).

[28] O. R. Enríquez, C. Hummelink, G.-W. Bruggert, D. Lohse, A. Prosperetti, D. van der Meer, and C. Sun, Growing bubbles in a slightly supersaturated liquid solution, Rev. Sci. Instrum. **84**, 065111 (2013).

[29] B.-S. Chun and G. T. Wilkinson, Interfacial tension in high-pressure carbon dioxide mixtures, Ind. Eng. Chem. Res. **34**, 4371 (1995).

[30] R. Sander, Compilation of Henry's law constants (version 4.0) for water as solvent, Atmos. Chem. Phys. **15**, 4399 (2015).

[31] A. Tamimi, E. B. Rinker, and O. C. Sandall, Diffusion coefficients for hydrogen sulfide, carbon dioxide, and nitrous oxide in water over the temperature range 293-368 K, J. Chem. Eng. Data **39**, 330 (1994).

[32] G. Ahlers, E. Bodenschatz, R. Hartmann, X. He, D. Lohse, P. Reiter, R. J. A. M. Stevens, R. Verzicco, M. Wedi, S. Weiss, X. Zhang, L. Zwirner, and O. Shishkina, Aspect Ratio Dependence of Heat Transfer in a Cylindrical Rayleigh-Bénard Cell, Phys. Rev. Lett. **128**, 084501 (2022).

[33] See Supplemental Material at http://link.aps.org/supplemental/10.1103/PhysRevFluids.8.093501 for videos of experiments (i)–(iv), experimental snapshots, propagation of projected front surfaces, and intensity and concentration profiles of experiments (v)–(xii) and the results of the. direct numerical simulations of case (B).

[34] N. Pande, S. K. Chandrasekar, D. Lohse, G. Mul, J. A. Wood, B. T. Mei, and D. Krug, Electrochemically induced pH change: Time-resolved confocal fluorescence microscopy measurements and comparison with numerical model, J. Phys. Chem. Lett. **11**, 7042 (2020).

[35] D. P. Faasen, D. van der Meer, D. Lohse, and P. Peñas, Slug bubble growth and dissolution by solute exchange, Phys. Rev. Fluids **6**, 113501 (2021).

[36] K. Tan and R. Thorpe, Gas diffusion into viscous and non-newtonian liquids, Chem. Eng. Sci. **47**, 3565 (1992).

[37] K.-K. Tan and R. B. Thorpe, The onset of convection induced by buoyancy during gas diffusion in deep fluids, Chem. Eng. Sci. **54**, 4179 (1999).

[38] K. K. Tan and R. B. Thorpe, The onset of convection caused by buoyancy during transient heat conduction in deep fluids, Chem. Eng. Sci. **51**, 4127 (1996).

[39] E. M. Sparrow, R. J. Goldstein, and V. K. Jonsson, Thermal instability in a horizontal fluid layer: Effect of boundary conditions and non-linear temperature profile, J. Fluid Mech. **18**, 513 (1964).

[40] R. Verzicco and P. Orlandi, A finite-difference scheme for three-dimensional incompressible flows in cylindrical coordinates, J. Comput. Phys. **123**, 402 (1996).

[41] E. A. Fadlun, R. Verzicco, P. Orlandi, and J. Mohd-Yusof, Combined immersed-boundary finite-difference methods for three-dimensional complex flow simulations, J. Comput. Phys. **161**, 35 (2000).

[42] R. Hartmann, R. Verzicco, L. Klein Kranenbarg, D. Lohse, and R. J. Stevens, Multiple heat transport maxima in confined-rotating Rayleigh–Bénard convection, J. Fluid Mech. **939**, A1 (2022).

[43] M. Holzner and B. Lüthi, Laminar Superlayer at the Turbulence Boundary, Phys. Rev. Lett. **106**, 134503 (2011).

[44] M. Wolf, B. Lüthi, M. Holzner, D. Krug, W. Kinzelbach, and A. Tsinober, Investigations on the local entrainment velocity in a turbulent jet, Phys. Fluids **24**, 105110 (2012).

[45] C. Dopazo, J. Martín, and J. Hierro, Iso-scalar surfaces, mixing and reaction in turbulent flows, C. R. Mec. **334**, 483 (2006).

[46] N. Chakraborty and R. S. Cant, A priori analysis of the curvature and propagation terms of the flame surface density transport equation for large eddy simulation, Phys. Fluids **19**, 105101 (2007).

[47] D. Krug, M. Holzner, B. Lüthi, M. Wolf, W. Kinzelbach, and A. Tsinober, The turbulent/non-turbulent interface in an inclined dense gravity current, J. Fluid Mech. **765**, 303 (2015).

[48] M. van Reeuwijk and M. Holzner, The turbulence boundary of a temporal jet, J. Fluid Mech. **739**, 254 (2014).

[49] O. Shishkina, Rayleigh-Bénard convection: The container shape matters, Phys. Rev. Fluids **6**, 090502 (2021).